CHEMISTRY OF MATERIALS
Cite This: Chem. Mater. XXXX, XXX, XXX−XXX
Article
pubs.acs.org/cm

Defect Engineering of Earth-Abundant Solar Absorbers BiSI and BiSeI

Alex M. Ganose,[†,‡,§] Saya Matsumoto,[†] John Buckeridge,[†] and David O. Scanlon*[,†,‡,§]

[†]Department of Chemistry, University College London, 20 Gordon Street, London WC1H 0AJ, U.K.
[‡]Thomas Young Centre, University College London, Gower Street, London WC1E 6BT, U.K.
[§]Diamond Light Source Ltd., Diamond House, Harwell Science and Innovation Campus, Didcot, Oxfordshire OX11 0DE, U.K.

Supporting Information

ABSTRACT: Bismuth-based solar absorbers have recently garnered attention due to their promise as cheap, nontoxic, and efficient photovoltaics. To date, however, most show poor efficiencies far below those seen in commercial technologies. In this work, we investigate two such promising materials, BiSI and BiSeI, using relativistic first-principles methods with the aim of identifying their suitability for photovoltaic applications. Both compounds show excellent optoelectronic properties with ideal band gaps and strong optical absorption, leading to high predicted device performance. Using defect analysis, we reveal the electronic and structural effects that can lead to the presence of deep trap states, which may help explain the prior poor performance of these materials. Crucially, detailed mapping of the range of experimentally accessible synthesis conditions allows us to provide strategies to avoid the formation of killer defects in the future.

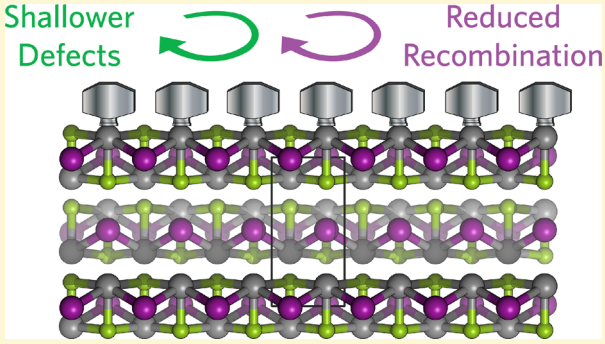

INTRODUCTION

Solar power currently presents the most attractive low-carbon alternative to fossil fuels, in part due to the vast amount of energy the sun provides, which dwarfs the total known supplies of oil, coal, and gas.[1,2] Furthermore, as the cost of solar devices continues to diminish, photovoltaics (PV) offer the highest technical potential of any renewable energy resource and suggest an attainable route to curbing climate change.[3] Indeed, the once aspirational 2020 cost target of $1.00 per W for solar technologies, set by US Department of Energy in 2011,[4] may now be in reach. If PV is to compete in utility-scale power generation, however, a further increase in cost-competitiveness will be necessary. A recent report suggests a long-term target of $0.25 per W by 2050 is essential for solar to reach 30% market penetration, presenting a significant challenge to the PV community.[5]

While the price of silicon-based devices has fallen steadily over the past decade, this is largely the result of optimized manufacturing processes and increased economies of scale with the underlying efficiency of panels remaining roughly unchanged.[6,7] A further reduction in price per W is limited by the fundamental cost of producing silicon wafers, which is unlikely to change after 60 years of development in the transistor industry, and the requirement of relatively thick films due to silicon's poor optical absorption.[8] Third-generation solar absorbers present an exciting alternative with increased efficiency, roll-to-roll printing, and the use of lightweight flexible substrates offering routes to reduced costs.[5,9,10]

Any new solar absorber must show efficient optoelectronic properties if it is to compete with existing technologies.[11] This includes a direct band gap between 1.1−1.5 eV, strong onset of optical absorption above the band gap to ensure effective collection of visible light, small charge-carrier effective masses to promote mobile charge transport, and defect tolerance to prevent unwanted recombination of photogenerated carriers. Other factors, such as the availability and cost of raw materials, and compatibility with commonly used hole and electron contact materials,[12] will further dictate market viability.

The lead hybrid halide perovskites have recently emerged as possible contenders to commercial silicon technologies.[13,14] Their rapid development, reaching 22.7% power conversion efficiency within a decade,[15] can be attributed to a fortuitous combination of excellent optoelectronic properties.[16] Not only do they possess all the desired attributes described above but the strong spin−orbit interaction acting on Pb results in a "spin-split indirect gap", thought to reduce carrier recombination by a factor of 350%.[17] Accordingly, the prototypical hybrid halide solar absorber, $CH_3NH_3PbI_3$ ($MAPbI_3$), shows extremely long carrier-diffusion lengths resulting from large carrier lifetimes,[18] benign defect properties,[19] and excellent carrier mobilities.[20] Unfortunately, $MAPbI_3$ possesses poor chemical,[21] thermal,[22] and photostability[23] which, despite much research effort, has yet to be adequately addressed.[24]

The recent progress seen in the hybrid perovskites has sparked interest into other lone-pair containing materials (i.e., possessing a ns^2 electronic configuration), particularly those containing the

Received: March 16, 2018
Revised: May 14, 2018
Published: May 14, 2018

DOI: 10.1021/acs.chemmater.8b01135
Chem. Mater. XXXX, XXX, XXX−XXX

heavier post-transition metals such as Sb and Bi.[11,25−27] These materials are expected to show comparable absorber properties due to their soft polarizability—enabling large dielectric constants and efficient screening of charged defects—and large spin−orbit coupling effects, leading to increased conduction bandwidth and lower effective masses.

BiSI and BiSeI are two such materials that show promise for photovoltaic applications (Figure 1). Despite possessing indirect

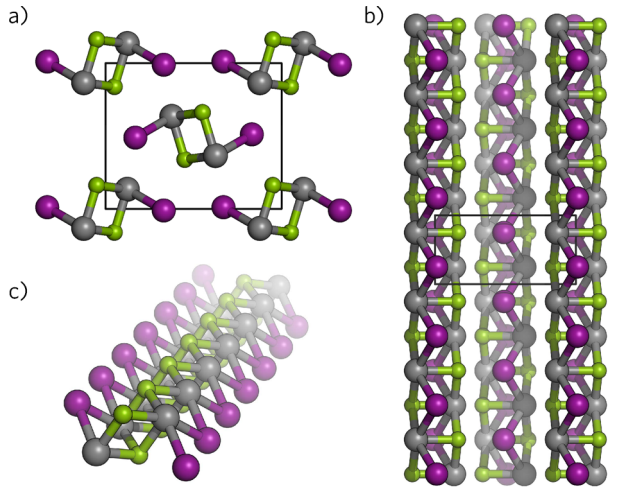

Figure 1. Crystal structure of BiSeI viewed along (a) the [100] direction and (b) the [001] direction. (c) A three-dimensional view, highlighting a single one-dimensional chain. Bi, Se, and I atoms are denoted by gray, green, and purple spheres, respectively.

fundamental band gaps, strong optical absorption is maintained by their slightly larger direct band gaps of 1.59 and 1.29 eV,[28] close to the ideal indicated by the Shockley−Quiesser limit.[29] In 2012, Hahn et al. produced solar cell devices containing both BiSI and $BiS_{1-x}Se_xI$ solid solutions but found poor performance in both cases.[30,31] Further research on BiSI remained limited until 2015, when a high-throughput screening identified BiSI and BiSeI as promising candidate photovoltaic absorbers due to their small density of states (DOS) effective masses and large ionic dielectric constants.[32] These properties, in addition to a valence band maximum composed of antibonding states, was proposed to provide a high level of defect tolerance, essential for an efficient solar absorber. A subsequent relativistic hybrid density functional theory (DFT) study indicated both compounds possessed ideal optoelectronic properties for solar absorbers, and attributed the limited performance of the cells produced by Hahn et al. to poor electronic alignment of the absorber to the hole and electron contact materials used.[29] Recent progress in low-temperature synthesis methods, enabling BiSI films with enhanced incident photon-to-current conversion efficiency (IPCE), further indicates the possibility of high-performance photovoltaics based on the bismuth chalcoiodides.[33]

In this work, we examine the optoelectronic properties of BiSI and BiSeI using quasiparticle self-consistent GW (QSGW) theory. Temperature-dependent effective masses, calculated within Boltzmann transport theory, are found to be relatively small in the directions of the 1D ribbons, indicating carriers should be mobile. Furthermore, strong optical absorption in combination with ideal band gaps results in high spectroscopically limited maximum efficiencies at small thin film thicknesses. We investigate the full range of intrinsic defects likely to form during equilibrium synthesis conditions. On the basis of this analysis, we identify regions of chemical potential space that may reduce the level of trap assisted recombination by $\sim 10^7$ cm^{-3} s^{-1}. Our results, therefore, may act as a guide to experimentalists attempting to produce more efficient bismuth chalcohalide-based photovoltaics.

COMPUTATIONAL METHODOLOGY

Geometry optimizations and defect energy calculations were performed within the framework of density functional theory, using the Vienna ab initio Simulation Package (VASP).[34−37] Convergence with respect to *k*-point sampling and plane wave energy were tested with a 3 × 6 × 2 Γ-centered mesh and 400 eV cutoff found to converge the total energy to 1 meV/Atom, for the 12 atom primitive cells of BiSI and BiSeI. Complete structural optimization of the lattice parameters and atomic positions was performed, such that the force on each atom totalled less than 0.01 eV $Å^{-1}$ with a larger cutoff energy of 520 eV used to avoid basis set errors arising from Pulay stress.[38]

Geometry optimizations were performed using the PBEsol functional,[39] a version of the Perdew Burke and Ernzerhof (PBE) functional[40] revised for solids. PBEsol has been shown to accurately reproduce the structure parameters of many materials containing weak dispersive interactions (such as those seen across the $[BiSI]_\infty$ chains) without requiring an additional dispersion correction.[41−44] Ionic contributions to the static dielectric constants were calculated using the PBEsol functional using density functional perturbation theory (DFPT)[45] with a 8 × 14 × 6 Γ-centered *k*-point mesh necessary to reach convergence. The calculated dielectric constants and Born effective charges are provided in Table S1 of the Supporting Information.

Defects were calculated in a 2 × 3 × 1 (72 atom) supercell using the PBEsol functional with a 2 × 3 × 3 *k*-point mesh. The PBEsol functional reproduces the experimental band gaps of BiSI and BiSeI, thereby negating the need to extrapolate the defect energies to account for band gap underestimation. We note, however, that PBEsol can suffer from the self-interaction error, which may cause unwanted delocalization of defect states. While fully ionized defects (i.e., those with no excess electrons or holes) will not be affected, partially ionized or un-ionized defects may be artificially stabilized by this delocalization.[46] The formation energy, ΔH_f, of a defect, *D*, with charge state, *q*, was calculated as

$$\Delta H_f^{D,q} = (E^{D,q} - E^H) + \sum \{n_i(E_i + \mu_i)\} + q(E_F + \varepsilon_v^H) + E_{corr} \quad (1)$$

where $E^{D,q}$ is the energy of the defected supercell and E^H is the energy of the host supercell.[47,48] The second term represents the energy change due to the exchange of an atom, *i*, with a chemical reservoir: n_i is the number of atoms of each type exchanged, E_i is the element reference energy calculated from the element in its standard state, and μ_i is the chemical potential of the atom. ε_v^H represents the energy needed to add or remove an electron from the VBM to a Fermi reservoir—i.e., the eigenvalue of the VBM in the host—and E_F is the Fermi level relative to ε_v^H. E_{corr} is a correction applied to account for various limitations of the defect scheme used and is comprised of three terms:

$$E_{corr} = E_{potal} + E_{bf} + E_{icc} \quad (2)$$

where E_{potal} is a correction to align the electrostatic potential of the defected supercell to that of the host,[47,49] E_{bf} corrects the effects on the total energy of erroneous band filling,[47] and E_{icc} accounts for the unphysical defect−defect Coulombic interactions that occur between periodic images of charged defects due to finite supercell size effects.[50]

The thermodynamic transition level, $\varepsilon(D,q/q')$, defined as the energy at which the charge state of defect, *D*, spontaneously transforms from $q \leftrightarrow q'$, was calculated according to

$$\varepsilon(D, q/q') = \frac{E^{D,q} - E^{D,q'}}{q' - q} \quad (3)$$

DOI: 10.1021/acs.chemmater.8b01135
Chem. Mater. XXXX, XXX, XXX−XXX

The thermodynamic transition levels indicate whether a defect will act as a shallow or deep defect and can be measured experimentally through techniques such as deep-level transient spectroscopy.[48] The self-consistent Fermi level and defect concentrations were calculated using the SC-Fermi code.[51−53]

To obtain accurate optoelectronic properties, electron transport and optical absorption calculations were performed using relativistic quasi-particle self-consistent GW theory (QSGW),[54] as implemented in the all-electron (linear muffin-tin orbital basis) package Questaal.[55] Starting from wave functions obtained through local-density approximation (LDA) calculations, self-consistency of the quasi-particle states was obtained with the addition of spin−orbit coupling, as recently described for $MAPbI_3$[56] and the related antimony chalcohalides.[57] LDA calculations were performed on a 3 × 6 × 2 Γ-centered mesh with a smaller 2 × 5 × 2 mesh found to provide convergence of the QSGW results.

While generally providing significantly greater accuracy than density functional theory-based methods, QSGW has been shown to systematically overestimate the band gaps for a wide range of materials, including most semiconductors.[54] This is thought to derive from the lack of electron−phonon interactions and the absence of ladder diagrams coupling electrons and holes, leading to insufficient screening in the random phase approximation (RPA).[58] Inclusion of these effects will reduce band gap overestimation but is extremely computationally demanding. Here, we instead adopted the empirical hybrid QSGW (hQSGW) approach,[59] in which 80% of the QSGW self-energy is combined with 20% of the LDA potential. This method has been shown to provide significant improvements in the calculation of band gaps and band positions in a broad range of semiconductors.[59−61]

Carrier effective masses were calculated using the BoltzTraP code[62] based on calculations performed using hQSGW. Convergence of BoltzTraP properties necessitates very dense *k*-point meshes, especially for low carrier concentrations and temperatures, as considered here. Accordingly, a 24 × 40 × 20 *k*-point mesh was used in the hQSGW calculations of electronic and optical properties.

RESULTS

BiSI and BiSeI crystallize in the orthorhombic *Pnma* space group, in which $[BiChI]_\infty$ ribbons are held together by weak van der Waals-type interactions (Figure 1).[63,64] The quasi-one-dimensional ribbons are formed of distorted edge-sharing pseudo-octahedra, comprising 3 Bi−Ch and 2 Bi−I bonds with the Bi lone pair occupying the vacant site. Geometry relaxations, performed using the PBEsol functional, were found to result in lattice constants in good agreement with experiment (full results provided in Table S2 of the Supporting Information).

BiSI and BiSeI possess complex electronic structures with many band extrema, often located away from high-symmetry points in the Brillouin zone (presented in Figure S1 of the Supporting Information).[29] Accordingly, conventional band structures along typical high-symmetry paths are not sufficient to accurately determine intrinsic electronic properties such as the fundamental band gap and charge carrier effective masses. In this report, we calculated these properties based on extremely dense sampling of the Brillouin zone to ensure predictive capability versus experiment. The band gaps of BiSI and BiSeI, calculated using hQSGW, were found to be 1.76 and 1.50 eV, respectively, in close agreement with previous hybrid DFT results (Table 1).[29] We note that the difference between indirect and direct band gaps is very small (0.02 eV in both cases), indicating the indirect nature will have minimal effect on optical absorption. Both compounds show a relatively strong temperature dependence on the size of the band gap ($dE_g/dT = -7.0 \times 10^{-4}$ eV K^{-1} for BiSI and -6.5×10^{-4} eV K^{-1} for BiSeI),[65] likely due to the weak forces holding the BiChI ribbons together, which allow for significant thermal expansion. As the hQSGW results do not take into account thermal effects, we therefore calculated the room temperature (293 K) band gaps based on the above corrections. The temperature corrected band gaps of 1.56 eV (BiSI) and 1.31 eV (BiSeI) are in good agreement with the room temperature experimental optical band gaps of 1.56−1.59 and 1.29−1.32 eV, respectively,[28,65] highlighting the accuracy of the hQSGW approach. Unlike the hybrid perovskites, in which spin-splitting of the band edges is thought to significantly reduce radiative recombination, the band structures of BiSI and BiSeI do not show any Rashba-type effects.[17] Regardless, the slightly indirect nature of the fundamental band gap is expected to result in lower radiative recombination rates.

Table 1. Fundamental Band Gaps of BiSI and BiSeI Obtained Using Different Methods[a]

compound	E_g^{HSE}	E_g^{hQSGW}	$E_g^{hQSGW,RT}$	E_g^{exp}
BiSI	1.78	1.76	1.56	1.56−1.59
BiSeI	1.52	1.50	1.31	1.29−1.32

[a] E_g^{HSE} gives the 0 K band gap (with the omission of zero point motion), calculated using the HSE06 functional,; E_g^{hQSGW} is the 0 K hybrid quasi-particle self-consistent GW (hQSGW) result, and $E_g^{hQSGW,RT}$ is the hQSGW result extrapolated to room temperature (293 K). All calculated results explicitly include spin−orbit coupling. E_g^{exp} gives the range of experimental band gaps, obtained from refs 28 and 65.

Carrier Effective Masses. To assess the suitability of BiSI and BiSeI for photovoltaic applications, carrier transport properties were investigated using the Boltztrap code. As the solutions to the Boltzmann transport equations are dependent on both carrier concentration and temperature, calculation of these properties allows for the effect of different doping regimes and device operating conditions to be evaluated. In solar absorbers, the antagonistic dependence of minority carrier concentration and diffusion length with regard to open-circuit voltage generally results in an optimal carrier concentration of $\sim 10^{16}-10^{17}$ cm^{-3} to prevent recombination losses. The charge-carrier effective masses of BiSI and BiSeI, taking into account a carrier concentration of 10^{16} cm^{-3} and representative device operating temperature of 293 K, are provided in Table 2. The 1D crystal structure results in effective masses that are strongly anisotropic: the electron effective masses are smallest in the directions parallel to the axis of the ribbons (along [010]), while the hole masses show an inverted trend with the [001] direction (spanning across the ribbons) showing the lightest masses, indicating that considerable interactions between the chains must be present.

Table 2. Effective Masses of Electrons (m_e^*) and Holes (m_h^*) in BiSI and BiSeI Calculated Using hQSGW and the BoltzTraP Code[a]

	m_e^*			m_h^*		
compound	*x*	*y*	*z*	*x*	*y*	*z*
BiSI	2.33	0.30	0.72	2.66	0.79	0.61
BiSeI	1.61	0.30	0.94	1.79	0.84	0.81

[a] Results provided in units of the electron rest mass, m_0.

In both BiSI and BiSeI, the effective masses of electrons are smaller than those of holes, as seen in other bismuth chalcogenide and halide-based semiconductors.[66,67] We note that these values deviate considerably from the effective masses calculated based on parabolic fitting of the band structure,

DOI: 10.1021/acs.chemmater.8b01135
Chem. Mater. XXXX, XXX, XXX−XXX

which indicate holes as the lighter of the two charge carriers,[11] thus highlighting the limitations of this approach in treating complex band structures with multiple band extrema. The small electron effective masses in the direction parallel to the 1D ribbons of 0.30 m_0 for both BiSI and BiSeI indicate that electrons should be fairly mobile and contrast favorably to other third-generation solar absorbers such as CuZnSnS (m_e^* = 0.18 m_0)[68] and $MAPbI_3$ (m_e^* = 0.15 m_0).[16]

Optical Properties. A key property to consider when screening a novel photovoltaic is its ability to absorb visible light; specifically, a strong onset of absorption up to ~10^5 cm^{-1} just above the band gap is essential to maximize the collection of incident solar radiation.[11] The 0 K optical absorption spectra of BiSI and BiSeI, calculated using hQSGW, are shown in Figure 2a. As expected, the onset of absorption is lower in BiSeI, in line with its smaller band gap. Both are excellent absorber materials with large optical absorption coefficients of greater than 1 × 10^5 cm^{-1} seen roughly 0.5 eV above the absorption edge. Such strong absorption can be attributed, in part, to the large density of states present at the band edges.[29]

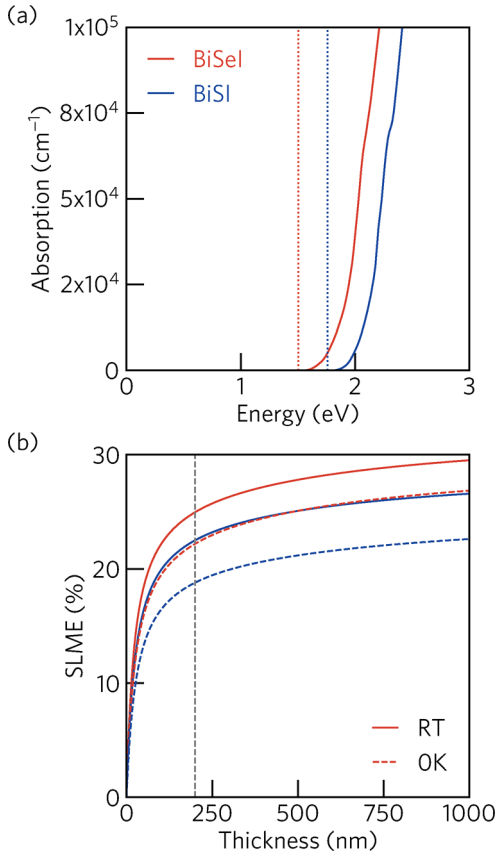

Figure 2. (a) 0 K optical absorption of BiSI (blue) and BiSeI (red), calculated using hQSGW. Fundamental band gaps (E_g^{hQSGW}) indicated by dotted lines. (b) SLME of BiSI and BiSeI, calculated using the 0 K band gaps and optical absorption (dashed lines) and results extrapolated to room temperature (solid lines).

The spectroscopically limited maximum efficiency (SLME) metric, proposed in 2012 by Yu and Zunger, provides an indication of the maximum possible efficiency of a solar absorber, considering the strength of optical absorption, nature of the band gap (direct versus indirect), and film thickness.[69,70] The effect of film thickness on SLME is presented in Figure 2b, calculated using both the 0 K hQSGW band gaps (E_g^{hQSGW}) and absorption coefficients, and results extrapolated to room temperature ($E_g^{hQSGW,RT}$). The smaller band gap (closer to the optimum indicated by the Shockley−Queisser limit) of BiSeI enables a larger SLME of 25.0% for a 200 nm film, compared to 22.5% for BiSI. These efficiencies are comparable to other thin-film absorbers such as CdTe (24.9%) and Cu_2ZnSnS_4 (25.7%) and, for the case of BiSeI, significantly greater than in $MAPbI_3$ (22.1%).[71]

Defect Chemistry. Based on our confirmation of the excellent optoelectronic properties of BiSI and BiSeI, we performed calculations to assess how the defect chemistry may affect device performance. The thermodynamically accessible range of chemical potentials (Figure S2 of the Supporting Information) indicates that both compounds are stable with the chemical potentials limited by formation of BiI_3 and the corresponding bismuth chalcogenide (Bi_2S_3 or Bi_2Se_3). The shape of the phase-stability region is similar in both cases, comprising a thin strip that spans a majority of the range of available chemical potentials. We accordingly identified two distinct synthesis environments for each compound, one which is anion-rich (S- and I-rich) and Bi-poor and expected to be optimum for *p*-type defect formation (A), and the other, which is anion-poor and Bi-rich (B) and expected to favor the formation of *n*-type defects.

The native *n*-type defects considered in this study include anion vacancies (V_{Ch} and V_I), anion on bismuth antisites (Ch_{Bi}, and I_{Bi}), the iodine on chalcogenide antisite (I_{Ch}), and the bismuth interstitial (Bi_i). Conversely, the *p*-type defects studied were the bismuth vacancy (V_{Bi}), bismuth on anion antisites (Bi_{Ch} and Bi_I), the chalcogenide on iodine antisite (Ch_I), and anion interstitials (Ch_i and I_i). Two potential interstitial defect sites were identified, comprising one octa-coordinated site and one penta-coordinated site (identified by superscript o and p, respectively), both present in the voids between the 1D ribbons (indicated in Figure S3 of the Supporting Information).

BiSI Defects. A plot of formation energy as a function of Fermi level for all intrinsic defects of BiSI calculated using PBEsol under the chosen chemical potential environments is shown in Figure 3. For clarity, the vacancy and antisite defects are plotted separately from the interstitials. Under the most *p*-type conditions (environment A), S_I is the lowest energy intrinsic acceptor with a relatively shallow 0/−1 transition level 0.14 eV above the VBM. The S_I acceptor defect is compensated by I_S and V_I, which acts to pin the Fermi level deep in the band gap. Indeed, using the calculated defect formation energies to determine the Fermi level self-consistently (at a temperature of 300 K) reveals it is trapped at 0.77 eV above the valence band maximum, leading to a hole concentration of 1.21 × 10^8 cm^{-3}.

The other *p*-type antisite defects show significantly higher formation energies (around 3 eV for the neutral charge states) and are therefore unlikely to be present in significant concentrations, especially considering the low processing temperature for BiSI films.[72] Of the interstitial defects, the I_i^o, S_i^p, and S_i^o can all act as acceptor defects, albeit at Fermi levels close to the CBM. Considering that the Fermi level under environmental conditions A will be pinned midgap, the interstitial defects are unlikely to play a role in *p*-type conductivity.

We note that the S_{Bi} and S_i^o donor defects possess ultradeep transition levels just above the VBM, which can act as charge recombination centers and severely compromise *p*-type conductivity. However, the incredibly low concentration of these defects (5.8 × 10^1 and 0.8 × 10^1 cm^{-3}, respectively, at a device operating temperature of 21 °C) indicates the effect on conductivity should be minimal.

DOI: 10.1021/acs.chemmater.8b01135
Chem. Mater. XXXX, XXX, XXX−XXX

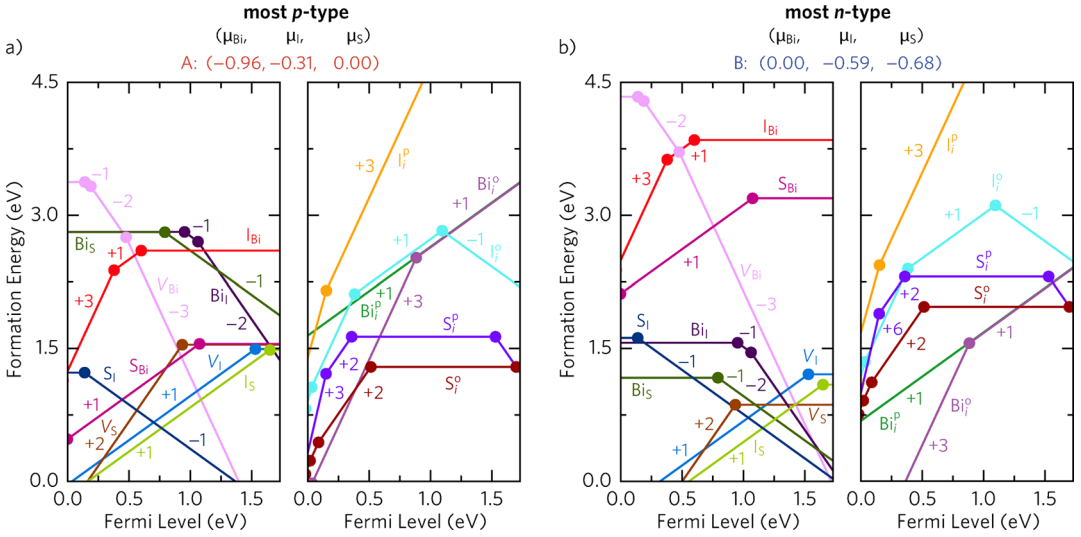

Figure 3. Defect transition level diagram for BiSI under (a) a p-type (Bi-poor, S- and I-rich) chemical potential environment and (b) an *n*-type (Bi-rich, S- and I-poor) chemical potential environment. The slope of the lines denotes the charge state with a steeper line indicating a higher charge state. The solid dots represent the transition levels, $\epsilon(q/q')$.

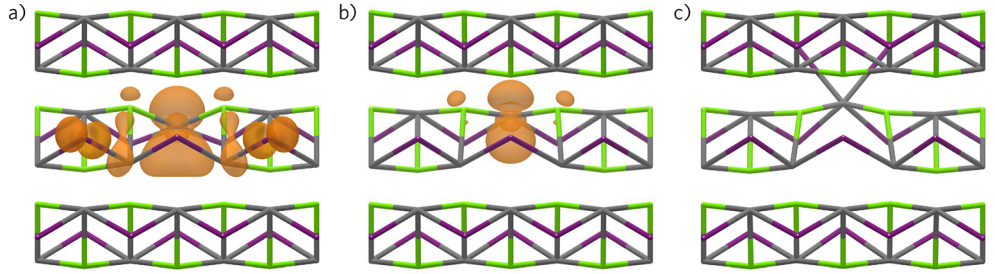

Figure 4. Crystal structure and charge density isosurfaces of the V_S defect in the (a) neutral, (b) +1, and (c) +2 charge states, viewed along the [001] direction. Green, gray, and purple cylinders indicate bonding to sulfur, bismuth, and iodine atoms, respectively. Electron density represented in orange. The isosurface level was set to 0.03 eV Å^{-3}.

Under the most *n*-type conditions (environment B), the lowest energy donor defect, I_S, possesses a shallow +1/0 transition level 0.08 eV below the CBM. Similar to the *p*-type environment, the Fermi level is pinned midgap (0.57 eV below the CBM) by compensation with the S_I^{-1} acceptor defect. V_I is the next most stable donor defect but shows a slightly deeper +1/0 transition level 0.20 eV from the band edge. In comparison, the neutral V_S is lower in energy than the neutral V_I; however, V_S is a negative-U defect with a 2+/0 transition state ultradeep within the gap (0.80 eV below the CBM), which can act as a charge trap and recombination center. This behavior arises from the stability of the neutral charge state, in which the two excess electrons are delocalized over the Bi sites adjacent to the vacancy such that the majority of the charge density fills the void in the structure (Figure 4a). To stabilize the charge density, the Bi atom opposite the vacant S site is pulled toward the vacancy, leaving the remainder of the 1D chain largely unaffected. In the +1 charge state, the electron is localized on a single adjacent Bi atom with considerably less electron density filling the vacancy site (Figure 4b). This causes the Bi atoms either side of the S vacancy to displace laterally, resulting in a structural deformation that propagates along the 1D chain, increasing the strain in the lattice and raising the defect formation energy. For the +2 charge state, the Bi atom opposite the defect site is pulled toward two iodine atoms in an adjacent chain, resulting in similar lattice deformation but greater overall stability (Figure 4c).

Of the *n*-type interstitials, the Bi_i^o defect is lowest in energy and possesses an ultradeep +1/+3 transition level. However, all interstitials will be present in very low concentrations due to their large formation energies at the self-consistent Fermi level. We note that both Bi_S and V_S are low energy defects with deep transition levels which can act as charge recombination centers. To alleviate any detrimental effects on *n*-type conductivity, postannealing in a sulfur atmosphere may be required to fill these defect sites.

BiSeI Defects. BiSeI shows a defect chemistry similar to that of its sulfur analogue. A plot of formation energy as a function of Fermi level for all intrinsic defects of BiSeI under the chosen chemical potential environments is shown in Figure 5. At the most type conditions (environment A), the lowest energy acceptor defect, Se_I, is lower in energy than the corresponding S_I and marginally shallower, resulting in a transition level 0.13 eV above the valence band. It is compensated by the Se_I defect, which acts to pin the Fermi level 0.68 eV above the valence band, resulting in a hole concentration of 8.52×10^7 cm^{-3} at room temperature.

In comparison to the *p*-type BiSI defects, the main difference is the considerably lower formation energy of Se_{Bi} (resulting in a large defect concentration of 4.77×10^{10} cm^{-3}), which may act as a charge recombination center due to its ultradeep 0/+1 transition level. Again, the other antisite and interstitial defects are much higher in energy and will only be present in very small concentrations.

DOI: 10.1021/acs.chemmater.8b01135
Chem. Mater. XXXX, XXX, XXX−XXX

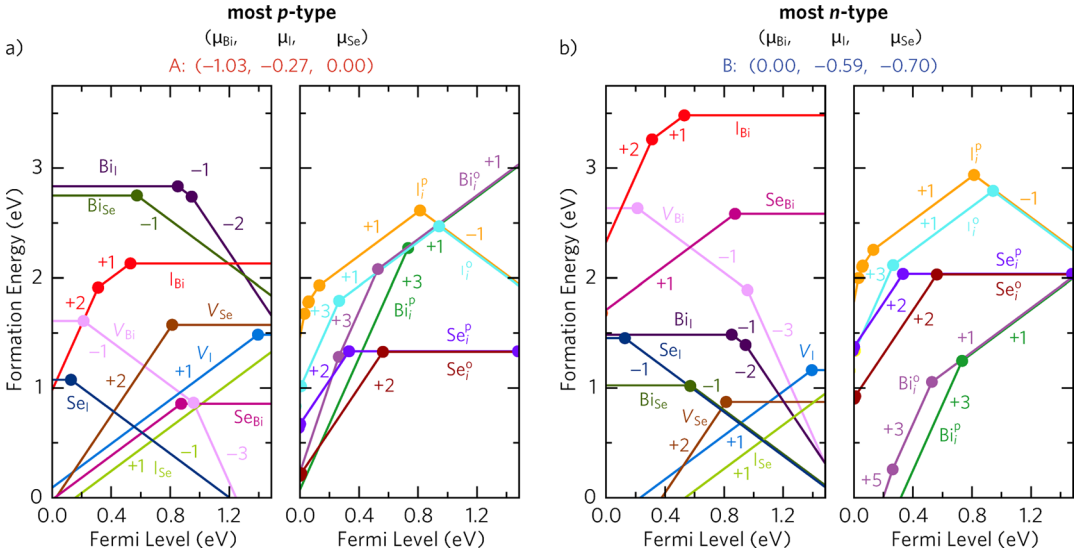

Figure 5. Defect transition level diagram for BiSeI under (a) a p-type (Bi-poor, Se- and I-rich) chemical potential environment and (b) an *n*-type (Bi-rich, Se- and I-poor) chemical potential environment. The slope of the lines denotes the charge state with a steeper line indicating a higher charge state. The solid dots represent the transition levels, $\varepsilon(q/q')$.

For the most *n*-type conditions (environment B), the donor defects are slightly shallower due to a lowered conduction band minimum based on band alignments relative the vacuum level.[29] The lowest energy donor is the I_{Se} defect with a transition level resonant in the conduction band (0.17 eV above the CBM), which is compensated concomitantly by Se_I and Be_{Se}. This traps the Fermi level 0.43 eV below the conduction band minimum, resulting in an electron concentration of 7.64×10^{11} cm^{-3} at room temperature.

Both V_{Se} and Bi_{Se} are again low energy ultradeep defects with concentrations of 1.17×10^{7} and 4.84×10^{12} cm^{-3}, respectively. Consequently, while V_{Se} will be less problematic than its counterpart in BiSI, annealing in a selenium atmosphere may be necessary to reduce the effects of Bi_{Se} on carrier recombination. For all interstitial defects, their high formation energy precludes their formation at device operating temperatures.

Defect Engineering. Due to the trapping of the Fermi level mid gap, both BiSI and BiSeI will act as intrinsic semiconductors, regardless of synthesis conditions, and are best suited to use in a *p*−*i*−*n* junction solar cell architecture. On the basis of the analysis of the above transition level diagrams, under the limits of and n-type conditions, deep defects such as Ch_{Bi} and V_{Ch} will dominate, resulting in high concentrations of deep trap states that may contribute to charge carrier recombination. With this in mind, we explored the full chemical potential space with the aim of minimizing the concentration of deep defects that may negatively impact carrier transport and recombination. At each point within the region of stability in chemical potential space (Figure S2 of the Supporting Information), we calculated the self-consistent Fermi level and corresponding defect concentrations. An estimate of the recombination rate was then calculated at each set of chemical potentials within a Shockley−Reed−Hall recombination model[73] (expected to comprise the majority of carrier recombination due to the low carrier concentrations) using the defect concentrations obtained in the previous step. Within this model, the recombination rate R^{SRH} depends on the charge carrier and defect concentrations in addition to the positions of the defect transition levels (a full description of the model is provided in the Supporting Information).

In the Shockley−Read−Hall model, defects with transition levels closer to the middle of the band gap will show considerably greater activity as recombination centers than those with transition levels close to the band edges. Accordingly, as the concentrations of deep versus shallow defects varies across chemical potential space, the rate of recombination can also be tuned. We note that, due to the computational difficulty in determining defect charge-capture cross sections from first-principles,[74] our model assumes a constant value for all defects ($\sigma = 1 \times 10^{-15}$ cm^2) and will therefore provide only a qualitative estimate of the true Shockley−Read−Hall recombination rate.

The recombination rate across the range of accessible chemical potentials for BiSI and BiSeI is shown in Figure 6. The rate has been normalized to the region of lowest recombination, as to indicate which areas of chemical potential space are likely to result in increased recombination. For BiSI, *p*-type conditions show the lowest recombination rate due to the relatively high formation energy of the dominant deep defects (S_{Bi} and V_S), resulting in low concentrations of these defects, in comparison to the total number of charge carriers. Moving to more *n*-type conditions, the rate of recombination increases gradually to over 10^{7} s^{-1} more than that of the most *p*-type environment, due to the lowering in energy of the ultradeep V_S and Bi_S defects. Accordingly, Bi-poor conditions are essential to reduce the effect of unwanted recombination on open-circuit voltage in functioning photovoltaic devices.

For BiSeI, the limits of the *p*- and *n*-type environments both show high levels of recombination. This can be ascribed to the to the low formation energy of the Se_{Bi} defect, dominating in *p*-type conditions, and the Bi_{Se} and V_{Se} defects found under *n*-type conditions, all of which show ultradeep transition levels. However, away from the chemical potential limits, the recombination rate drops sharply due to fewer low-energy trap states (Figure S4 of the Supporting Information). As such, a more balanced stoichiometric ratio of starting materials should be used to reduce the concentration of killer defects. We note that the differences in the recombination rate behavior between BiSI and BiSeI may have implications for alloys of the two materials, as recently proposed as a way of tuning the optical band gap for improved photovoltaic performance.[30,75]

DOI: 10.1021/acs.chemmater.8b01135
Chem. Mater. XXXX, XXX, XXX−XXX

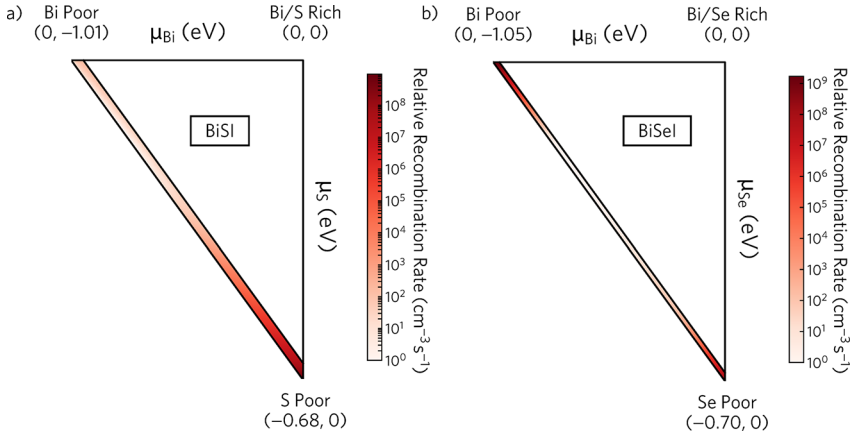

Figure 6. Shockley–Read–Hall recombination rate (R^{SRH}) across the range of accessible chemical potentials for (a) BiSI and (b) BiSeI. Greater levels of recombination are indicated by darker regions of red.

CONCLUSIONS

We have demonstrated using relativistic quasi-particle self-consistent GW theory the potential of BiSI and BiSeI as earth-abundant photovoltaics. Investigations into their optoelectronic properties indicates small electron effective masses in the directions of the BiChI chains, coupled with extremely strong optical absorption just above the fundamental band gap. We have predicted a large SLME of 25.0 and 22.5% for BiSeI and BiSI, respectively, competitive with the best current generation photovoltaic absorbers. Defect analysis reveals both compounds are intrinsic semiconductors and are best suited for use in *p–i–n* junction devices. Furthermore, mapping of the chemical potential space identifies regions likely to show reduced recombination rates under accessible experimental conditions. We reveal that careful control over the elemental chemical potentials may enable a reduction in trap assisted recombination rates by $\sim 10^7$ cm^{-3} s^{-1}. Our research, therefore, can serve as a guide to experimentalists attempting to produce efficient bismuth chalcohalide-based photovoltaic absorbers.

ASSOCIATED CONTENT

Supporting Information

The Supporting Information is available free of charge on the ACS Publications website at DOI: 10.1021/acs.chemmater.8b01135.

Shockley–Read–Hall recombination rate methodology; calculated dielectric constants and Born effective charges; calculated lattice parameters; range of accessible chemical potentials; location of interstitial defect sites; defect transition level diagram of BiSeI at a point in the middle of the chemical potential stability region (PDF)

AUTHOR INFORMATION

Corresponding Author

*E-mail: d.scanlon@ucl.ac.uk.

ORCID

Alex M. Ganose: 0000-0002-4486-3321
John Buckeridge: 0000-0002-2537-5082
David O. Scanlon: 0000-0001-9174-8601

Notes

The authors declare no competing financial interest.

ACKNOWLEDGMENTS

This work made use of the ARCHER UK National Supercomputing Service (http://www.archer.ac.uk) via our membership in the UK's HEC Materials Chemistry Consortium, which is funded by EPSRC (EP/L000202) and the UCL Legion and Grace HPC Facilities. D.O.S. acknowledges support from the EPSRC (EP/N01572X/1). D.O.S. acknowledges support from the European Research Council, ERC, (Grant 758345). D.O.S. acknowledges membership of the Materials Design Network. J.B. acknowledges EPSRC support under Grant EP/K016288/1. A.M.G. acknowledges Diamond Light Source for the cosponsorship of a studentship on the EPSRC Centre for Doctoral Training in Molecular Modelling and Materials Science (EP/L015862/1).

REFERENCES

(1) Hermann, W. Quantifying global exergy resources. *Energy* **2006**, *31*, 1685–1702.
(2) Peter, L. M. Towards Sustainable Photovoltaics: The Search for New Materials. *Philos. Trans. R. Soc., A* **2011**, *369*, 1840–1856.
(3) Levelized Avoided Cost of New Generation Resources in the Annual Energy Outlook 2015, 2015. https://www.eia.gov/outlooks/aeo/pdf/electricity_generation.pdf (accessed February 28, 2018).
(4) US Department of Energy, 2015; https://energy.gov/sites/prod/files/2016/06/f32/SunShot-factsheet-6-10_final-508.pdf (accessed February 28, 2018).
(5) Sivaram, V.; Stranks, S. D.; Snaith, H. J. Perovskite solar cells could beat the efficiency of silicon. *Sci. Am.* **2015**, *1*.1
(6) Lacerda, J. S.; van den Bergh, J. C. Diversity in solar photovoltaic energy: Implications for innovation and policy. *Renewable Sustainable Energy Rev.* **2016**, *54*, 331–340.
(7) Rubin, E. S.; Azevedo, I. M.; Jaramillo, P.; Yeh, S. A review of learning rates for electricity supply technologies. *Energy Policy* **2015**, *86*, 198–218.
(8) Peng, J.; Lu, L.; Yang, H. Review On Life Cycle Assessment of Energy Payback and Greenhouse Gas Emission of Solar Photovoltaic Systems. *Renewable Sustainable Energy Rev.* **2013**, *19*, 255–274.
(9) Travis, W.; Knapp, C. E.; Savory, C. N.; Ganose, A. M.; Kafourou, P.; Song, X.; Sharif, Z.; Cockcroft, J. K.; Scanlon, D. O.; Bronstein, H.; Palgrave, R. G. Hybrid organic–inorganic coordination complexes as tunable optical response materials. *Inorg. Chem.* **2016**, *55*, 3393–3400.
(10) Ganose, A. M.; Cuff, M.; Butler, K. T.; Walsh, A.; Scanlon, D. O. Interplay of orbital and relativistic effects in bismuth oxyhalides: BiOF, BiOCl, BiOBr, and BiOI. *Chem. Mater.* **2016**, *28*, 1980–1984.
(11) Ganose, A. M.; Savory, C. N.; Scanlon, D. O. Beyond methylammonium lead iodide: prospects for the emergent field of ns^2 containing solar absorbers. *Chem. Commun.* **2017**, *53*, 20–44.
(12) Savory, C. N.; Ganose, A. M.; Travis, W.; Atri, R. S.; Palgrave, R. G.; Scanlon, D. O. An assessment of silver copper sulfides for photovoltaic applications: theoretical and experimental insights. *J. Mater. Chem. A* **2016**, *4*, 12648–12657.

DOI: 10.1021/acs.chemmater.8b01135
Chem. Mater. XXXX, XXX, XXX–XXX

(13) Green, M. A.; Ho-Baillie, A.; Snaith, H. J. The Emergence of Perovskite Solar Cells. *Nat. Photonics* **2014**, *8*, 506−514.
(14) Grätzel, M. The Light and Shade of Perovskite Solar Cells. *Nat. Mater.* **2014**, *13*, 838−842.
(15) Green, M. A.; Hishikawa, Y.; Dunlop, E. D.; Levi, D. H.; Hohl-Ebinger, J.; Ho-Baillie, A. W. Solar cell efficiency tables (version 51). *Prog. Photovoltaics* **2018**, *26*, 3−12. , PIP-17-216.
(16) Frost, J. M.; Butler, K. T.; Brivio, F.; Hendon, C. H.; van Schilfgaarde, M.; Walsh, A. Atomistic Origins of High-Performance in Hybrid Halide Perovskite Solar Cells. *Nano Lett.* **2014**, *14*, 2584−2590.
(17) Azarhoosh, P.; McKechnie, S.; Frost, J. M.; Walsh, A.; Van Schilfgaarde, M. Research Update: Relativistic origin of slow electron-hole recombination in hybrid halide perovskite solar cells. *APL Mater.* **2016**, *4*, 091501.
(18) Stranks, S. D.; Eperon, G. E.; Grancini, G.; Menelaou, C.; Alcocer, M. J.; Leijtens, T.; Herz, L. M.; Petrozza, A.; Snaith, H. J. Electron-hole diffusion lengths exceeding 1 micrometer in an organometal trihalide perovskite absorber. *Science* **2013**, *342*, 341−344.
(19) Walsh, A.; Scanlon, D. O.; Chen, S.; Gong, X. G.; Wei, S.-H. Self-Regulation Mechanism for Charged Point Defects in Hybrid Halide Perovskites. *Angew. Chem.* **2015**, *127*, 1811−1814.
(20) Oga, H.; Saeki, A.; Ogomi, Y.; Hayase, S.; Seki, S. Improved understanding of the electronic and energetic landscapes of perovskite solar cells: high local charge carrier mobility, reduced recombination, and extremely shallow traps. *J. Am. Chem. Soc.* **2014**, *136*, 13818−13825.
(21) Niu, G.; Guo, X.; Wang, L. Review of recent progress in chemical stability of perovskite solar cells. *J. Mater. Chem. A* **2015**, *3*, 8970−8980.
(22) Juarez-Perez, E. J.; Hawash, Z.; Raga, S. R.; Ono, L. K.; Qi, Y. Thermal degradation of $CH_3NH_3PbI_3$ perovskite into NH_3 and CH_3I gases observed by coupled thermogravimetry−mass spectrometry analysis. *Energy Environ. Sci.* **2016**, *9*, 3406−3410.
(23) Brivio, F.; Caetano, C.; Walsh, A. Thermodynamic origin of photoinstability in the $CH_3NH_3Pb(I_{1-x}Br_x)_3$ hybrid halide perovskite alloy. *J. Phys. Chem. Lett.* **2016**, *7*, 1083−1087.
(24) Wang, Z.; Ganose, A. M.; Niu, C.; Scanlon, D. O. First-principles insights into tin-based two-dimensional hybrid halide perovskites for photovoltaics. *J. Mater. Chem. A* **2018**, *6*, 5652−5660.
(25) Lehner, A. J.; Wang, H.; Fabini, D. H.; Liman, C. D.; Hébert, C.-A.; Perry, E. E.; Wang, M.; Bazan, G. C.; Chabinyc, M. L.; Seshadri, R. Electronic Structure and Photovoltaic Application of BiI_3. *Appl. Phys. Lett.* **2015**, *107*, 131109.
(26) Lehner, A. J.; Fabini, D. H.; Evans, H. A.; Hébert, C.-A.; Smock, S. R.; Hu, J.; Wang, H.; Zwanziger, J. W.; Chabinyc, M. L.; Seshadri, R. Crystal and Electronic Structures of Complex Bismuth Iodides $A_3Bi_2I_9$ (A= K, Rb, Cs) Related to Perovskite: Aiding the Rational Design of Photovoltaics. *Chem. Mater.* **2015**, *27*, 7137−7148.
(27) Savory, C. N.; Ganose, A. M.; Scanlon, D. O. Exploring the $PbS-Bi_2S_3$ series for next generation energy conversion materials. *Chem. Mater.* **2017**, *29*, 5156−5167.
(28) Shin, D.-W.; Hyun, S.-C.; Park, S.-a.; Kim, Y.-G.; Kim, C.-d.; Kim, W.-T. Optical properties of undoped and Ni-doped V^A-VI^A-VII^A single crystals. *J. Phys. Chem. Solids* **1994**, *55*, 825−830.
(29) Ganose, A. M.; Butler, K. T.; Walsh, A.; Scanlon, D. O. Relativistic electronic structure and band alignment of BiSI and BiSeI: candidate photovoltaic materials. *J. Mater. Chem. A* **2016**, *4*, 2060−2068.
(30) Hahn, N. T.; Rettie, A. J.; Beal, S. K.; Fullon, R. R.; Mullins, C. B. n-BiSI Thin Films: Selenium Doping and Solar Cell Behavior. *J. Phys. Chem. C* **2012**, *116*, 24878−24886.
(31) Hahn, N. T.; Self, J. L.; Mullins, C. B. BiSI Micro-Rod Thin Films: Efficient Solar Absorber Electrodes? *J. Phys. Chem. Lett.* **2012**, *3*, 1571−1576.
(32) Brandt, R. E.; Stevanović, V.; Ginley, D. S.; Buonassisi, T. Identifying Defect-Tolerant Semiconductors with High Minority-Carrier Lifetimes: Beyond Hybrid Lead Halide Perovskites. *MRS Commun.* **2015**, *5*, 265−275.
(33) Kunioku, H.; Higashi, M.; Abe, R. Low-Temperature Synthesis of Bismuth Chalcohalides: Candidate Photovoltaic Materials with Easily, Continuously Controllable Band gap. *Sci. Rep.* **2016**, *6*, 32664.
(34) Kresse, G.; Hafner, J. *Ab Initio* Molecular Dynamics for Liquid Metals. *Phys. Rev. B: Condens. Matter Mater. Phys.* **1993**, *47*, 558−561.
(35) Kresse, G.; Hafner, J. *Ab Initio* Molecular-Dynamics Simulation of the Liquid-Metal Amorphous-Semiconductor Transition in Germanium. *Phys. Rev. B: Condens. Matter Mater. Phys.* **1994**, *49*, 14251−14269.
(36) Kresse, G.; Furthmüller, J. Efficient Iterative Schemes for *Ab Initio* Total-Energy Calculations Using a Plane-Wave Basis Set. *Phys. Rev. B: Condens. Matter Mater. Phys.* **1996**, *54*, 11169−11186.
(37) Kresse, G.; Furthmüller, J. Efficiency of *Ab Initio* Total Energy Calculations for Metals and Semiconductors Using a Plane Wave Basis Set. *Comput. Mater. Sci.* **1996**, *6*, 15−50.
(38) Pulay, P. Ab initio calculation of force constants and equilibrium geometries in polyatomic molecules: I. Theory. *Mol. Phys.* **1969**, *17*, 197−204.
(39) Perdew, J. P.; Ruzsinszky, A.; Csonka, G. I.; Vydrov, O. A.; Scuseria, G. E.; Constantin, L. A.; Zhou, X.; Burke, K. Restoring the Density-Gradient Expansion for Exchange in Solids and Surfaces. *Phys. Rev. Lett.* **2008**, *100*, 136406.
(40) Perdew, J. P.; Burke, K.; Ernzerhof, M. Generalized Gradient Approximation Made Simple. *Phys. Rev. Lett.* **1996**, *77*, 3865−3868.
(41) Ganose, A. M.; Gannon, L.; Fabrizi, F.; Nowell, H.; Barnett, S. A.; Lei, H.; Zhu, X.; Petrovic, C.; Scanlon, D. O.; Hoesch, M. Local corrugation and persistent charge density wave in $ZrTe_3$ with Ni intercalation. *Phys. Rev. B: Condens. Matter Mater. Phys.* **2018**, *97*, 155103.
(42) Ganose, A. M.; Savory, C. N.; Scanlon, D. O. Electronic and defect properties of $(CH_3NH_3)_2Pb(SCN)_2I_2$ analogues for photovoltaic applications. *J. Mater. Chem. A* **2017**, *5*, 7845−7853.
(43) Biswas, D.; Ganose, A. M.; Yano, R.; Riley, J.; Bawden, L.; Clark, O.; Feng, J.; Collins-Mcintyre, L.; Sajjad, M.; Meevasana, W.; Hoesch, M.; Rault, J.; Sasagawa, T.; Scanlon, D.; King, P. Narrow-band anisotropic electronic structure of ReS_2. *Phys. Rev. B: Condens. Matter Mater. Phys.* **2017**, *96*, 085205.
(44) Björkman, T.; Gulans, A.; Krasheninnikov, A.; Nieminen, R. Are we van der Waals ready? *J. Phys.: Condens. Matter* **2012**, *24*, 424218.
(45) Wu, X.; Vanderbilt, D.; Hamann, D. Systematic treatment of displacements, strains, and electric fields in density-functional perturbation theory. *Phys. Rev. B: Condens. Matter Mater. Phys.* **2005**, *72*, 035105.
(46) Peng, H.; Scanlon, D. O.; Stevanovic, V.; Vidal, J.; Watson, G. W.; Lany, S. Convergence of density and hybrid functional defect calculations for compound semiconductors. *Phys. Rev. B: Condens. Matter Mater. Phys.* **2013**, *88*, 115201.
(47) Lany, S.; Zunger, A. Assessment of correction methods for the band-gap problem and for finite-size effects in supercell defect calculations: Case studies for ZnO and GaAs. *Phys. Rev. B: Condens. Matter Mater. Phys.* **2008**, *78*, 17−20.
(48) Freysoldt, C.; Grabowski, B.; Hickel, T.; Neugebauer, J.; Kresse, G.; Janotti, A.; Van De Walle, C. G. First-principles calculations for point defects in solids. *Rev. Mod. Phys.* **2014**, *86*, 253−305.
(49) Freysoldt, C.; Neugebauer, J.; Van de Walle, C. G. Fully ab initio finite-size corrections for charged-defect supercell calculations. *Phys. Rev. Lett.* **2009**, *102*, 016402.
(50) Murphy, S. T.; Hine, N. D. M. Anisotropic charge screening and supercell size convergence of defect formation energies. *Phys. Rev. B: Condens. Matter Mater. Phys.* **2013**, *87*, 094111.
(51) Buckeridge, J.; Jevdokimovs, D.; Catlow, C.; Sokol, A. Nonstoichiometry and Weyl fermionic behavior in TaAs. *Phys. Rev. B: Condens. Matter Mater. Phys.* **2016**, *94*, 180101.
(52) Taylor, F. H.; Buckeridge, J.; Catlow, C. R. A. Defects and oxide ion migration in the solid oxide fuel cell cathode material $LaFeO_3$. *Chem. Mater.* **2016**, *28*, 8210−8220.

DOI: 10.1021/acs.chemmater.8b01135
Chem. Mater. XXXX, XXX, XXX−XXX

(53) Buckeridge, J. SC-Fermi. https://github.com/jbuckeridge/sc-fermi (accessed February 28, 2018).
(54) van Schilfgaarde, M.; Kotani, T.; Faleev, S. Quasiparticle Self-Consistent GW Theory. *Phys. Rev. Lett.* **2006**, *96*, 226402.
(55) Questaal. www.questaal.org (accessed February 27, 2018).
(56) Brivio, F.; Butler, K. T.; Walsh, A.; Van Schilfgaarde, M. Relativistic quasiparticle self-consistent electronic structure of hybrid halide perovskite photovoltaic absorbers. *Phys. Rev. B: Condens. Matter Mater. Phys.* **2014**, *89*, 155204.
(57) Butler, K. T.; McKechnie, S.; Azarhoosh, P.; Van Schilfgaarde, M.; Scanlon, D. O.; Walsh, A. Quasi-particle electronic band structure and alignment of the V-VI-VII semiconductors SbSI, SbSBr, and SbSeI for solar cells. *Appl. Phys. Lett.* **2016**, *108*, 112103.
(58) Kotani, T.; van Schilfgaarde, M.; Faleev, S. V. Quasiparticle self-consistent GW method: A basis for the independent-particle approximation. *Phys. Rev. B: Condens. Matter Mater. Phys.* **2007**, *76*, 165106.
(59) Deguchi, D.; Sato, K.; Kino, H.; Kotani, T. Accurate energy bands calculated by the hybrid quasiparticle self-consistent GW method implemented in the ecalj package. *Jpn. J. Appl. Phys.* **2016**, *55*, 051201.
(60) Svane, A.; Christensen, N. E.; Cardona, M.; Chantis, A. N.; van Schilfgaarde, M.; Kotani, T. Quasiparticle self-consistent *GW* calculations for PbS, PbSe, and PbTe: Band structure and pressure coefficients. *Phys. Rev. B: Condens. Matter Mater. Phys.* **2010**, *81*, 245120.
(61) Bakhtatou, A.; Meddour, A. Quasiparticle self-consistent GW study of AlN. *Phys. Status Solidi B* **2016**, *253*, 442−449.
(62) Madsen, G. K. H.; Singh, D. J. BoltzTraP. A code for calculating band-structure dependent quantities. *Comput. Phys. Commun.* **2006**, *175*, 67−71.
(63) Demartin, F.; Gramaccioli, C.; Campostrini, I. Demicheleite-(I), BiSI, a New Mineral from La Fossa Crater, Vulcano, Aeolian Islands, Italy. *Mineral. Mag.* **2010**, *74*, 141−145.
(64) Braun, T. P.; DiSalvo, F. J. Bismuth Selenide Iodide. *Acta Crystallogr., Sect. C: Cryst. Struct. Commun.* **2000**, *56*, iuc9900177−e2.
(65) Chepur, D.; Bercha, D.; Turyanitsa, I.; Slivka, V. Y. Peculiarities of the Energy Spectrum and Edge Absorption in the Chain Compounds $A^{V}B^{VI}C^{VII}$. *Phys. Status Solidi B* **1968**, *30*, 461−468.
(66) Micic, O.; Li, Z.; Mills, G.; Sullivan, J.; Meisel, D. Formation of Small Particles of Lead Iodide, Mercuric Iodide, and Bismuth Iodide Layered Semiconductors. *J. Phys. Chem.* **1987**, *91*, 6221−6229.
(67) Guo, D.; Hu, C.; Zhang, C. First-Principles Study on Doping and Temperature Dependence of Thermoelectric Property of Bi_2S_3 Thermoelectric Material. *Mater. Res. Bull.* **2013**, *48*, 1984−1988.
(68) Liu, H.-R.; Chen, S.; Zhai, Y.-T.; Xiang, H.-J.; Gong, X.-G.; Wei, S.-H. First-principles study on the effective masses of zinc-blend-derived $Cu_2Zn-IV-VI_4$ (IV= Sn, Ge, Si and VI= S, Se). *J. Appl. Phys.* **2012**, *112*, 093717.
(69) Yu, L.; Zunger, A. Identification of potential photovoltaic absorbers based on first-principles spectroscopic screening of materials. *Phys. Rev. Lett.* **2012**, *108*, 068701.
(70) Yu, L.; Kokenyesi, R. S.; Keszler, D. A.; Zunger, A. Inverse Design of High Absorption Thin-Film Photovoltaic Materials. *Adv. Energy Mater.* **2013**, *3*, 43−48.
(71) Unpublished results provided by internal correspondence with C. N. Savory. University College London, February 28, 2018.
(72) Brandt, R. E.; Poindexter, J. R.; Gorai, P.; Kurchin, R. C.; Hoye, R. L.; Nienhaus, L.; Wilson, M. W.; Polizzotti, J. A.; Sereika, R.; Zaltauskas, R.; Lee, L. C.; MacManus-Driscoll, J. L.; Bawendi; Stevanovic, V.; Buonassisi, T. Searching for defect-tolerant photovoltaic materials: combined theoretical and experimental screening. *Chem. Mater.* **2017**, *29*, 4667−4674.
(73) Shockley, W.; Read, W., Jr Statistics of the recombinations of holes and electrons. *Phys. Rev.* **1952**, *87*, 835.
(74) Alkauskas, A.; Dreyer, C. E.; Lyons, J. L.; Van de Walle, C. G. Role of excited states in Shockley-Read-Hall recombination in wide-band-gap semiconductors. *Phys. Rev. B: Condens. Matter Mater. Phys.* **2016**, *93*, 201304.
(75) Groom, R. A.; Jacobs, A.; Cepeda, M.; Drummey, R.; Latturner, S. E. Structural and Optical Properties of Sb-Substituted BiSI Grown from Sulfur/Iodine Flux. *Inorg. Chem.* **2017**, *56*, 12362−12368.

DOI: 10.1021/acs.chemmater.8b01135
Chem. Mater. XXXX, XXX, XXX−XXX